Laser powder bed fusion spatters of Zr-Cu-Al-Nb metallic glass

Camille Pauzon, Rémi Daudin, Florence Robaut, Grégory Berthomé, Jean-Jacques Blandin

Journal of Alloys and Compounds 976 (2024) 173073

Contents lists available at ScienceDirect

Journal of Alloys and Compounds

journal homepage: www.elsevier.com/locate/jalcom

Laser powder bed fusion spatters of Zr-Cu-Al-Nb metallic glass

Camille Pauzon *, Rémi Daudin, Florence Robaut, Grégory Berthomé, Jean-Jacques Blandin

University Grenoble Alpes, CNRS, Grenoble INP, SIMaP, Grenoble 38000, France

ARTICLE INFO

Keywords:
Laser powder bed fusion
Bulk metallic glasses
Spatters
Crystallisation
Lack-of-fusion defect

ABSTRACT

Understanding the morphology, composition and structural changes experienced by metallic glass powder particles upon laser powder bed fusion (LPBF) is the first step towards evaluating the impact of spatter generation on part quality and on feedstock degradation. This study presents the characterization of Zr-Cu-Al-Nb spatter particles by means of scanning and transmission electron microscopy with automated crystallographic orientation mapping and energy dispersive spectroscopy, and X-ray photoelectron spectroscopy. The powder exposed to the LPBF environment exhibits an average surface composition similar to the original feedstock, but with a rougher morphology. The typical spatter encountered in the remaining lack-of-fusion is a vapour-entrained particle, which probably underwent partial melting leading to the formation of α-Zr(O) dendrites, and "big-cube" Cu_2Zr_4O nanocrystals in its heat affected zone. In the present work, spatter characteristics are discussed considering glass properties and their connection to lack-of-fusion defects is addressed.

1. Introduction

Additive Manufacturing of metallic glass alloys by laser powder bed fusion (LPBF) is promising to push the size and complexity limits of conventional casting. The high cooling rates allow to by-pass crystallisation upon solidification. However, the subsequent layer melting leads to cyclic reheating of the already deposited material. While this can be exploited for texture control in traditional crystalline materials [1], it is for metallic glasses a devitrification hazard. To tackle this additional processing constraint, the widespread approach is to work at laser power typically below 100 W, to limit the heat affected zone (HAZ) [2]. Process parameter and strategy optimisations can significantly cut down the lack-of-fusion (l-o-f) defects population; however, spatters may be an additional barrier to the densification [3]. While spatters resulting from metallic glass LPBF have not been studied, the literature on spatters of traditional crystalline alloys gives an overview of crystalline spatter properties.

Spatters are LPBF by-products generated either, from direct melt pool ejections, or vapour-driven particle entrainment from the powder bed [4]. Depending on the alloy, process conditions and the spatter origin, these ejections may be more or less oxidised [5], with morphologies and microstructures differing from the virgin powder [5,6]. Ly et al. [4] distinguished between hot and cold entrained particles, hot particles being partially to fully remelted while cold particles may have experience only minor heating. With high speed imaging and particle image velocimetry monitoring LPBF of 316 L stainless steel, these authors showed that hot entrained particles account for 60% of total spatter generation, cold particles for 25% and direct melt pool ejections for 15%. While direct melt pool ejections are typically larger than the initial fresh powder, not necessarily as spherical and can lead to agglomerate formation when solidifying in flight, the entrained particles typically retain sizes similar to that of virgin powder [8].

The high temperatures and impurities the powder particles are exposed to during LPBF can trigger the mass transfer of elements of high affinity to oxygen from the volume to the surface of the particles. Different techniques have been developed to sample spatter particles to later analyse their surface chemistry, with techniques like X-ray photoelectron spectroscopy (XPS), such as the design of powder capsule. Chen et al. [9] showed the preferential oxidation of Al and Cr on the surface of Inconel 718 trapped in capsules with different built-in lattices and related the lattice density to the powder degradation. Other approaches consist in sampling spatter from regions where these do not mix with the powder bed. For example, Raza et al. [10] highlighted that Ti-6Al-4V spatters deposited in the LPBF machine gas outlet have a uniform Al-, Ti-based oxide layer with Al-rich oxide particulates growing on top. In case of AlSi10Mg, Raza et al. [7] showed the formation of a thick surface oxide, mainly Al_2O_3 with $MgAl_2O_4$ particulates at the topmost surface.

In terms of microstructural and morphological differences with virgin particles, crystalline spatters are not always easy to distinguish from

* Corresponding author.
E-mail address: camille.pauzon@simap.grenoble-inp.fr (C. Pauzon).

https://doi.org/10.1016/j.jallcom.2023.173073
Received 30 August 2023; Received in revised form 8 November 2023; Accepted 6 December 2023
Available online 7 December 2023

the rest of the powder bed. In case of direct melt pool ejections, melt flow features can be preserved after solidification, and for Inconel 718, their cross-sections can reveal a finer microstructure than that of the virgin particles, suggesting higher cooling rates than upon atomization [8].

Redeposited spatters can affect the local layer thickness, chemistry, and in case of metallic glasses, the local material structure, leading to potential local segregations and l-o-f defects. As shown by Sohrabi et *al.* [11], l-o-f defects are harmful to the as-built strength and the toughness of the $Zr_{59.3}Cu_{28.8}Al_{10.4}Nb_{1.5}$ alloy. It is thus primordial to understand the origin of the spatter formation during LPBF of metallic glasses and their properties, keeping in mind redeposition issues and recyclability perspectives. In the context of metallic glasses, the present work evaluates spatter properties to identify possible composition and structural changes from the fresh feedstock that may alter the glass forming ability and its LPBF processability.

2. Materials and methods

Laser powder bed fusion of powder with nominal composition $Zr_{59.3}Cu_{28.8}Al_{10.4}Nb_{1.5}$ in at% (Amloy-Zr01, Hereaus), was conducted on an EOS M290 machine. Parts were produced with an energy density of 18 J/mm^3 (i.e. scan speed of 1700 mm/s, laser power of 90 W, hatch distance of 0.15 mm) on a Ti-6Al-4V grade 5 baseplate with 20 μm thick layers, up to a height of 9 mm. The achieved relative density is 99.9% measured by X-ray tomography with an EASYTOM XL Nanofocus (RX Solutions), and a 6.4 μm voxel size, and thus only defects larger than 18 μm are detected. Powder samples were collected from the virgin feedstock, the powder bed after printing, and the deposits within the gas outlet of the machine. The gas outlet is a socket system to catch the protective gas flow stream and direct it to the filter system. The particles entrained by the gas flow and deposited in this gas outlet are spatter particles generated at the laser - powder bed interaction area [8]. Thus, analysing these deposits allows grasping the characteristics of spatter particles independently, without mixing with feedstock powder. These spatter particles represent the fraction of the overall spatter population whose trajectories reached the gas outlet, i.e. for a great part, coming from the parts closest to the gas outlet. One should bear in mind that spatter particles redeposit also on the powder bed. To limit to the greatest extent the harmful redeposition of spatter, a part exposure strategy consisting in scanning parts closest to the gas outlet first was adopted.

The surface morphology and microstructure of the powder samples were analysed by SEM with a Zeiss GeminiSEM 500 FEG SEM. To characterize the cross-sections of powder particles representative of the virgin powder and spatters, focused ion beam milling to extract lamellas from the particles surface was performed with a Thermo Fisher Helios 5 PlasmaFIB SEM. The lifted out lamellas were thinned down following a conventional transmission electron microscopy lamella preparation [12]. In more details, these were PFIB prepared at 30 kV, using an over-tilt angle of 2°, a first 1 nA-polishing step and a final one at 100 pA. The samples were studied with a TEM JEOL 2100 and analysed by EDS, operating at 200 kV. The mapping of an ROI was recorded with a 1 nm probe size and a 2 nm step size. The nature and orientation of the observed phases within these were retrieved by ACOM (Automated Crystallographic Orientation Mapping) [13], with ASTAR™ from Nanomegas.

The surface chemistry of the powder samples was studied by X-ray Photoelectron Spectroscopy (XPS) using a Thermo Scientific™ K-Alpha™ system, equipped with a monochromatic Al Kα source for the generation of the photoelectrons. The analysed area was about 400 μm in diameter. Therefore, many particles were analysed at the same time providing with an average representative result of the powder surface state of each sample. High-resolution scans covering the binding energies of the elements of interest (i.e. Zr3d, Cu2p, Al2p, Nb3d, O1s) were performed. To correct any charging effect, the binding energies were calibrated to the C1s level of adventitious carbon at 285.0 eV. The overall oxygen content of the virgin powder and of the powder collected on the baseplate were measured by combustion gas analysis using a LECO O836.

3. Results and discussion

Processing of Zr-based metallic glass at moderate energy, in comparison to other metallic materials, to by-pass crystallisation is associated with the presence of l-o-f defects in the as-built material, see Fig. 1a-b). While number of such defects are systematic and associated with insufficient energy to bond adjacent laser tracks and subsequent layers, a close examination of large flaws reveals the presence of partially melted and enclosed powder particles with rough surface morphologies. In contrast, the virgin particles have smooth surfaces, see Fig. 1c-d). The particles found in the l-o-f defects have surfaces exhibiting pits and crevices analogous to that of spatter particles collected in the gas outlet, see yellow arrows in Fig. 1a-b,e-f). One should bear in mind that particles collected from the gas outlet only come from spatter generation and are not mixed with particles from the powder bed.

These observations are consistent with the connection drawn between spatter particles and l-o-f occurrence in the literature. This relationship was identified for crystalline metallic alloys by combining in situ monitoring and ex situ X-ray tomography [3,14,15]. In addition, with relevance to the present work, Khairallah et *al.* [16] underlined that moderate power processing favours spatter redeposition rather than generation, which is difficult to anticipate and harmful.

The most common spatter particles encountered here have an uneven surface as depicted in Fig. 1e-f). With a lower frequency, some agglomerates are also noted, alongside another type of particles, seldom observed and identified as direct melt pool ejections (Fig. S1). Herein, these direct melt pool ejections, also called “recoil pressure induced droplet breakup ejections” in [4], are exceptional and not observed within l-o-f defects. In addition, their large size ensures their removal upon sieving. Minute amount of such ejections is consistent with the observations of Ly et *al.* [4], who reported that these represent about 15% of all 316 L stainless steel spatters. The rest is owing to metal vapour-induced particle entrainment, and accordingly, the rough spatter particles are categorized as such.

In the atomisation context, the high viscosity of the metallic glass results in the formation of a small amount of filament and elongated powder particles retained after sieving (Fig. S2). In the LPBF context, the high viscosity works against the Marangoni convective flow, thereby limiting the forces against the surface tension and hence the generation of direct melt pool ejections. To understand the changes spatters have undergone, thereafter, the present study focuses on entrained spatter particles, as seen in Fig. 1f).

FIB lamellas were taken from the surface of such particle and from a representative one from the virgin feedstock. The BF-STEM image and SAED pattern taken in the virgin lamella confirm the amorphous nature of the feedstock, Fig. 2a), also verified by XRD (Fig. S3). In contrast, the spatter particle has experienced complex structural changes in its volume, see Fig. 2b). Closer to its surface (few μm in depth), the formation of coarse structures surrounded by the amorphous matrix is visible, while the particle core is populated by nanocrystals. The latter recall the nanocrystals found in the HAZ of the same alloy produced by LPBF [2], although presently larger. To identify the nature of these crystals, ACOM analysis in these two regions was performed, see Fig. 3.

The ACOM analysis confirms the formation of coarse dendrites close to the particle surface, with a single common orientation corresponding to the hexagonal α-Zr(O) phase enriched in oxygen, see Fig. 3a-c). This α-Zr(O) phase is the stable structure of pure Zr at low to intermediate temperatures, and can dissolve up to 35 at% oxygen [17]. Herein, the dendrites are decorated with smaller crystals of tetragonal $CuZr_2$ and cubic oxide Cu_2Zr_4O. The latter is also known as the “big-cube” phase, whose crystallisation is promoted by small amount of oxygen impurities in Zr-based amorphous alloys [18]. This is consistent with the presence of 620 ± 9 ppm oxygen in the virgin powder measured by LECO. The

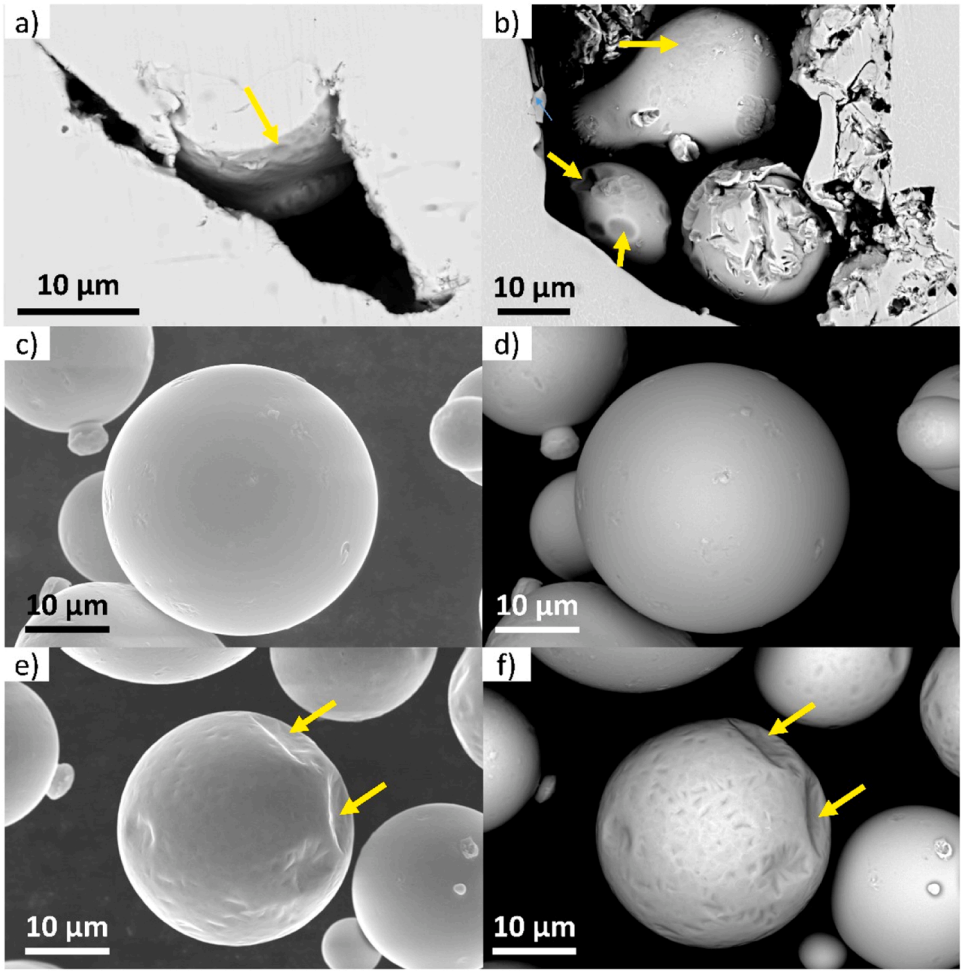

Fig. 1. Micrographs of: a-b) Lack-of-fusion defects observed in as-built parts, connected to spatter particles, c-d) Virgin powder particle, e-f) Spatter particle collected in the gas outlet of the machine. a-d) and d-f) Images collected with BSE detector, c) and e) images with the SE in lens detector. The yellow arrows point out analogous surface features on the spatter particle and the particles within the l-o-f defects.

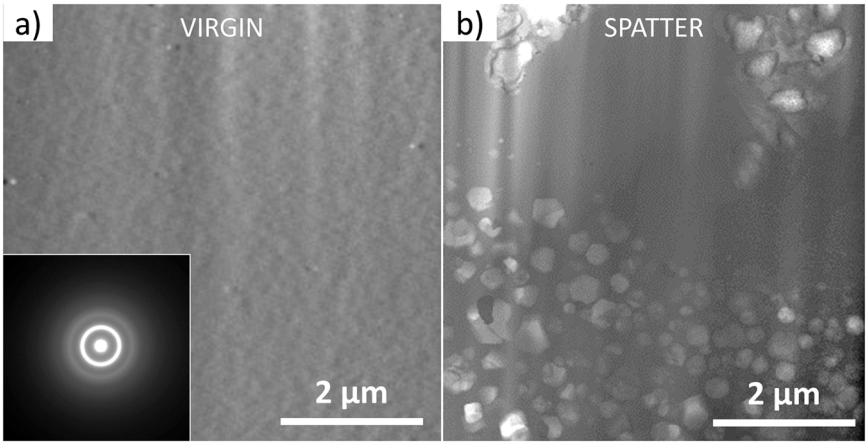

Fig. 2. a) BF STEM image of the lamella taken from the virgin particle, and insert of the associated SAED pattern. b) BF STEM image of the lamella taken from the spatter particle, where two distinct zones of crystallisation: close to the surface with coarse crystals and nanocrystals deeper in the volume.

$CuZr_2$ phase has already been identified in the LPBF and as-cast form of this alloy after annealing at 370 °C by XRD by Ericsson et *al.* [19], and upon continuous heating by Pacheco et *al.* [20]. These findings comply with the thermodynamic calculations of Zhou et *al.* [21] on Al-Cu-Zr showing that $CuZr_2$ is a stable phase for this system.

Marattukalam et *al.* [2] also reported the presence of α-Zr(O) in as-built parts, as a devitrification product alongside the "big-cube" phase. In their case, the size of the α-Zr(O) phase was only of about 100 nm without distinguishable dendritic microstructure. As shown by Trivedi and Laorchan [22], the crystal morphology formed in an

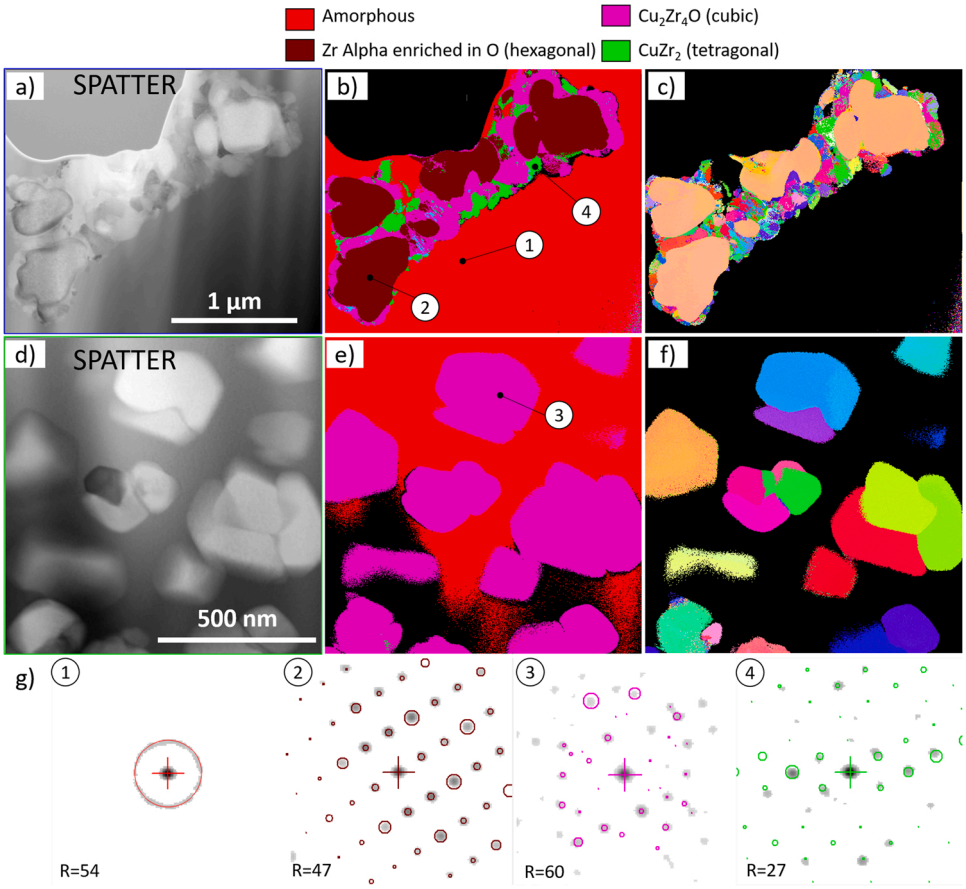

Fig. 3. Characterization of the spatter inner crystallisation with ACOM on the dendritic and nanocrystalline regions: a-d) BF STEM, b-e) Phase maps, c-f) Orientation maps particles, and g) selected diffraction patterns with the overlaid matching template and corresponding phase reliability index. Low phase reliability solutions are removed and appear in black in the maps.

amorphous matrix can vary from dendrites to small spherical crystals when increasing undercooling. The presence of dendrites close to the surface of the spatter suggests that the spatter was heated locally to temperatures allowing significant atomic diffusion, experiencing partial melting. In addition, these regions cooled down slower than the LPBF melt pool or upon atomisation, for which no such crystallisation is noted. Upon the formation of α-Zr(O), Cu is expected to be rejected into the glassy phase, and a new equilibrium is established between the dendrite and the matrix of new composition. This may induce the crystallisation of the two other Cu-rich phases at the dendrite – matrix interface. As emphasized by Marattukalam et *al.* [2], one can also suspect that the α-Zr(O) phase plays an important role on the formation of Cu_2Zr_4O, in a similar fashion as reported for the metastable Ni_2OZr_4 in the Zr-Al-Cu-Ni system [23,24]. Indeed, oxygen occupies the octahedral sites of the hexagonal lattice and is surrounded by 6 atoms, and hence it has the same coordination as in the "big-cube" Cu_2Zr_4O phase.

It should be pointed out that the dendrites decorated by $CuZr_2$ and Cu_2Zr_4O are surrounded by the amorphous matrix free of other phases. This absence of "big-cube" phase nanocrystals suggests that this region underwent solidification, rather than solid-state transformation. As exploited by Cheng et *al.* [25] for a Zr-Ti-Nb-Cu-Ni-Be, Zr phases like α-Zr(O) with high solubility of oxygen, may act as oxygen getters from the glass matrix upon solidification, which may further hinder the formation of "big-cube" nanocrystals.

The nanocrystals in the particle volume are also identified as the "big-cube" phase, see Fig. 3d-f). Previous work report the presence of similar "big-cube" nanocrystals in the as-built HAZ [2,26]. As reported by Barrico et *al.* [18], the microstructure of this phase can vary from coarse in thick ribbons and casting to nanocrystals in annealed fully amorphous materials. These elements suggest that the region displayed in Fig. 3e), is likely to have undergone solid-state transformation upon the vapour-induced particle entrainment.

These observations allow us to infer that the spatter particle has experienced a complex thermal history leading to the α-Zr(O) dendrite formation, probably originating from solidification of a melted region, concomitant to the growth of "big-cube" nanocrystals in the rest of the particle. The α-Zr(O) formation is suspected to be responsible for the spatter surface roughness which exhibits dendritic pattern (Fig. S4), although the connection is not yet fully elucidated. While solidification shrinkage can be ruled out as the α-Zr(O) and the amorphous matrix have similar densities (i.e., in the range 6.5–6.7 g/cm^3) These observations recall the work of Scheffler et al. [27] on surface crystallisation in which a "pulling-in" or "pushing-out" effect of the surface is caused by the crystallisation of different crystal faces.

The presence of l-o-f defects in connection to spatters redeposition may be severe for the present process, since the deposited layers are only 20 µm thick, in order to limit the laser energy necessary. Despite spatters of size similar to virgin particles, redeposition can lead to important local layer thickness variations. In addition, the crystalline phases formed in the spatter particle will melt at higher temperatures than the amorphous matrix and may act as a consolidation barrier. For example, it is interesting to point out that Yue et *al.* [28] had to use an energy density of 60 J/mm^3 for LPBF of pure Zr (i.e. about 3 times present energy), whose melting point is close to 1850 °C. Hence, one could think of scanning strategies including higher power remelting to remove spatter-related l-o-f. Once a larger volume of spatter particles is collected, future work will focus on processing the Zr-based glass with recycled powder.

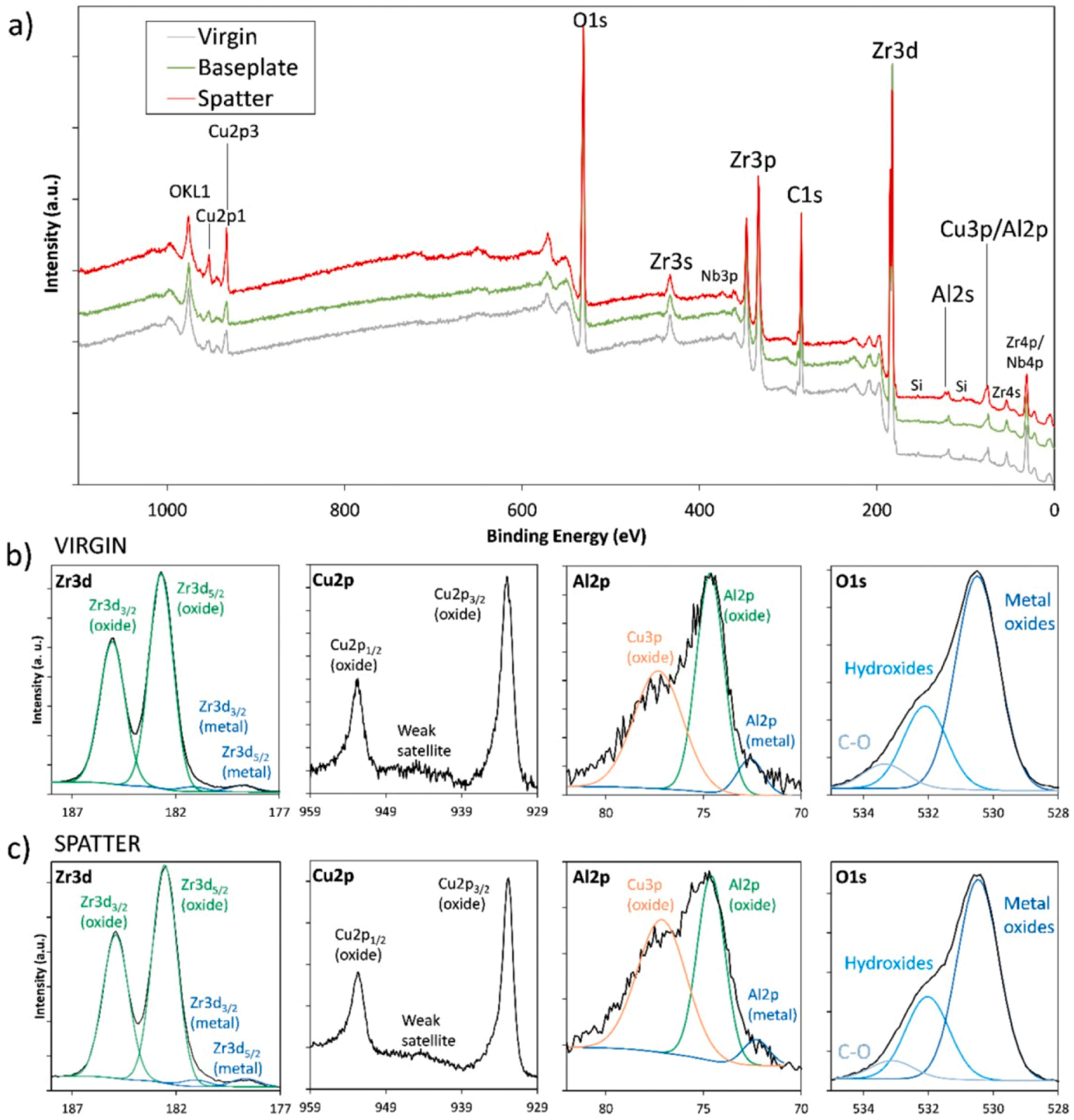

Fig. 4. XPS analysis of the virgin powder, of the powder on the baseplate collected after the print was completed, and of the spatter particles collected in the gas outlet: a) Survey spectra, and narrow scans on Zr3d, Cu2p, Al2p and O1s for b) the virgin and c) the spatter samples.

The XPS survey scans presented in Fig. 4a) highlight that the surface chemistry of the powder on the baseplate after printing is very similar to the virgin feedstock and to the collected spatters. In addition, the narrow scans on Zr3d allow the collection of the metallic and oxide contributions in similar ratios for the virgin and spatter samples. Hence, the surface oxide (i.e. oxide and hydroxide) is likely of the order of 10 nm for the two samples. This is consistent with the absence of obvious oxide features on the rough spatter particles in Fig. 1e-f). In addition, only a minor oxygen pick-up is measured in the powder sample collected from the baseplate, i.e. 642 ± 4 ppm. The narrow scans and corresponding peak fitting on the other main alloying elements enable to compare the oxide contributions of the three samples as reported in Table 1. It points out the enrichment in Cu of the surface oxide on spatters, with a ratio of normalised Cu to Zr oxide content in the spatter sample about twice that of the virgin one.

4. Conclusions

In summary, the spatter properties of the most commonly Zr-based metallic glass for LPBF were presented. The typical spatter type was

Table 1
Normalised cations concentrations from the fitting of the narrow scans, and ratios of cations for the virgin powder, the spatter particles collected in the gas outlet and the powder on the baseplate.

	Al ox %	Cu ox %	Zr ox %	Nb ox%	Cu ox/ Zr ox	Al ox/Cu ox	Al ox/ Nb ox
Virgin	0.3	47.6	49.5	2.6	1.0	0.007	0.1
Spatter	0.3	64.1	34.1	1.5	1.9	0.005	0.2
Baseplate	0.3	48.3	49.4	2.0	1.0	0.006	0.1

identified as entrained particles, which underwent complex heating upon ejection, resulting in α-Zr(O) dendrite crystallisation, alongside Cu_2Zr_4O "big-cube" nanocrystals formation. This work supports the next step consisting in evaluating the impact of the structural and chemical changes of the powder on the as-built material integrity.

CRediT authorship contribution statement

Camille Pauzon: Conceptualization; Formal analysis; Investigation; Writing - Original Draft; Visualization; Funding acquisition. **Rémi Daudin**: Conceptualization; Validation; Resources; Writing - Review & Editing; Supervision. **Florence Robaut**: Methodology; Investigation. **Grégory Berthomé**: Methodology; Investigation; Resources. **Jean-Jacques Blandin**: Conceptualization; Validation; Resources; Writing - Review & Editing; Supervision.

Declaration of Competing Interest

The authors declare that they have no known competing financial interests or personal relationships that could have appeared to influence the work reported in this paper.

Data Availability

Data will be made available on request.

Acknowledgments

Funded by the European Union under the grant agreement "ROSAMA2″ n°101059435 (MSCA-PF). Views and opinions expressed are however those of the author(s) only and do not necessarily reflect those of the European Union or REA. Neither the European Union nor the granting authority can be held responsible for them. This work also benefited from the investments made by the Center of Excellence of Multifunctional Architectured Materials "CEMAM" n°AN-10-LABX-44–01, and from the facilities available on the characterization platform CMTC of Grenoble INP-UGA.

Appendix A. Supporting information

Supplementary data associated with this article can be found in the online version at doi:10.1016/j.jallcom.2023.173073.

References

[1] H. Choo, K.L. Sham, J. Bohling, A. Ngo, X. Xiao, Y. Ren, P.J. Depond, M. J. Matthews, E. Garlea, Effect of laser power on defect, texture, and microstructure of a laser powder bed fusion processed 316L stainless steel, Mater. Des. 164 (2019) 1–12, https://doi.org/10.1016/j.matdes.2018.12.006.
[2] J.J. Marattukalam, V. Pacheco, D. Karlsson, L. Riekehr, J. Lindwall, F. Forsberg, U. Jansson, M. Sahlberg, B. Hjörvarsson, Development of process parameters for selective laser melting of a Zr-based bulk metallic glass, Addit. Manuf. 33 (2020) 1–8, https://doi.org/10.1016/j.addma.2020.101124.
[3] C. Schwerz, B.A. Bircher, A. Küng, L. Nyborg, In-situ detection of stochastic spatter-driven lack of fusion: Application of optical tomography and validation via ex-situ X-ray computed tomography, Addit. Manuf. 72 (2023) 1–13, https://doi.org/10.1016/j.addma.2023.103631.
[4] S. Ly, A.M. Rubenchik, S.A. Khairallah, G. Guss, J. Manyalibo, Metal vapor micro-jet controls material redistribution in laser powder bed fusion additive manufacturing, Sci. Rep. (2017) 1–12, https://doi.org/10.1038/s41598-017-04237-z.
[5] A. Raza, C. Pauzon, E. Hryha, A. Markström, P. Forêt, Spatter oxidation during laser powder bed fusion of Alloy 718: Dependence on oxygen content in the process atmosphere, Addit. Manuf. 48 (2021) 1–13, https://doi.org/10.1016/j.addma.2021.102369.
[6] A.N.D. Gasper, B. Szost, X. Wang, D. Johns, S. Sharma, A.T. Clare, I.A. Ashcroft, Spatter and oxide formation in laser powder bed fusion of Inconel 718, Addit. Manuf. 24 (2018) 446–456, https://doi.org/10.1016/j.addma.2018.09.032.
[7] A. Raza, T. Fiegl, I. Hanif, A. Markström, M. Franke, C. Körner, E. Hryha, Degradation of AlSi10Mg powder during laser based powder bed fusion processing, Mater. Des. 198 (2021) 1–12, https://doi.org/10.1016/j.matdes.2020.109358.
[8] C. Pauzon, A. Raza, E. Hryha, P. Forêt, Oxygen balance during laser powder bed fusion of Alloy 718, Mater. Des. 201 (2021) 1–10, https://doi.org/10.1016/j.matdes.2021.109511.
[9] Z. Chen, A. Raza, E. Hryha, Influence of part geometry on spatter formation in laser powder bed fusion of Inconel 718 alloy revealed by optical tomography, J. Manuf. Process 81 (2022) 680–695, https://doi.org/10.1016/j.jmapro.2022.07.031.
[10] A. Raza, C. Pauzon, S.D. Goff, E. Hryha, Effect of processing gas on spatter generation and oxidation of TiAl6V4 alloy in laser powder bed fusion process, Appl. Surf. Sci. 613 (2023), 156089, https://doi.org/10.1016/j.apsusc.2022.156089.
[11] N. Sohrabi, A. Parrilli, J. Jhabvala, A. Neels, R.E. Logé, Tensile and impact toughness properties of a zr-based bulk metallic glass fabricated via laser powder-bed fusion, Materials 14 (2021) 1–15, https://doi.org/10.3390/ma14195627.
[12] J. Mayer, L.A. Giannuzzi, T. Kamino, J. Michael, TEM sample preparation and FIB-induced damage, MRS Bull. 32 (2007) 400–407, https://doi.org/10.1557/mrs2007.63.
[13] E.F. Rauch, M. Véron, Automated crystal orientation and phase mapping in TEM, Mater. Charact. 98 (2014) 1–9, https://doi.org/10.1016/j.matchar.2014.08.010.
[14] Z. Snow, L. Scime, A. Ziabari, B. Fisher, V. Paquit, Observation of spatter-induced stochastic lack-of-fusion in laser powder bed fusion using in situ process monitoring, Addit. Manuf. 61 (2023) 1–14, https://doi.org/10.1016/j.addma.2022.103298.
[15] M.S. Palm, B. Diepold, S. Neumeier, H.W. Hoeppel, M. Goeken, M.F. Zaeh, Detection and effects of lack of fusion defects in Hastelloy X manufactured by laser powder bed fusion, Mater. Des. 230 (2023) 1–13, https://doi.org/10.1016/j.matdes.2023.111941.
[16] S.A. Khairallah, A.A. Martin, J.R.I. Lee, G. Guss, N.P. Calta, J.A. Hammons, M. H. Nielsen, K. Chaput, E. Schwalbach, M.N. Shah, M.G. Chapman, T.M. Willey, A. M. Rubenchik, A.T. Anderson, Y.M. Wang, M.J. Matthews, W.E. King, Controlling interdependent meso-nanosecond dynamics and defect generation in metal 3D printing, Science (1979) 368 (2020) 660–665. ⟨https://www.science.org⟩.
[17] J.-P. Abriata, J. Garcés, R. Versaci, The O-Zr (Oxygen-Zirconium) System, Bull. Alloy Phase Diagr. 7 (1986) 116–124.
[18] M. Baricco, S. Spriano, I. Chang, M.I. Petrzhik, L. Battezzati, "Big cube" phase formation in Zr-based metallic glasses, Mater. Sci. Eng. A304. 306 (2001) 305–310.
[19] A. Ericsson, V. Pacheco, J.J. Marattukalam, R.M. Dalgliesh, A.R. Rennie, M. Fisk, M. Sahlberg, Crystallization of a Zr-based metallic glass produced by laser powder bed fusion and suction casting, J. Non Cryst. Solids 571 (2021) 1–9, https://doi.org/10.1016/j.jnoncrysol.2021.120891.
[20] V. Pacheco, D. Karlsson, J.J. Marattukalam, M. Stolpe, B. Hjörvarsson, U. Jansson, M. Sahlberg, Thermal stability and crystallization of a Zr-based metallic glass produced by suction casting and selective laser melting, J. Alloy. Compd. 825 (2020) 1–8, https://doi.org/10.1016/j.jallcom.2020.153995.
[21] C. Zhou, C. Guo, C. Li, Z. Du, Thermodynamic assessment of the phase equilibria and prediction of glass-forming ability of the Al–Cu–Zr system, J. Non Cryst. Solids 461 (2017) 47–60, https://doi.org/10.1016/j.jnoncrysol.2016.09.031.
[22] R. Trivedi, V. Laorchan, Crystallization from an amorphous matrix-I. Morphological studies, Acta Metall. 36 (1988) 1941–1950, https://doi.org/10.1016/0001-6160(88)90296-9.
[23] A. Gebert, J. Eckert, L. Schultz, Effet of oxygen on phase formation and thermal stability of slowly cooled Zr65Al7.5Cu17.5Ni10 metallic glass, Acta Mater. 46 (1998) 5475–5482.
[24] J. Eckert, N. Mattern, M. Zinkevitch, M. Seidel, Crystallization behavior and phase formation in Zr-Al-Cu-Ni metallic glass containing oxygen, Mater. Trans. 39 (1998) 623–632.
[25] J.L. Cheng, G. Chen, C.T. Liu, Y. Li, Innovative approach to the design of low-cost Zr-based BMG composites with good glass formation, Sci. Rep. 3 (2013) 1–5, https://doi.org/10.1038/srep02097.
[26] J. Lindwall, A. Ericsson, J.J. Marattukalam, C.J. Hassila, D. Karlsson, M. Sahlberg, M. Fisk, A. Lundbäck, Simulation of phase evolution in a Zr-based glass forming alloy during multiple laser remelting, J. Mater. Res. Technol. 16 (2022) 1165–1178, https://doi.org/10.1016/j.jmrt.2021.12.056.
[27] F. Scheffler, M. Fleck, R. Busch, S. Casado, E. Gnecco, C. Tielemann, D.S. Brauer, R. Müller, Surface Crystallization of Barium Fresnoite Glass: Annealing Atmosphere, Crystal Morphology and Orientation, Cryst. (Basel) 13 (2023) 1–17, https://doi.org/10.3390/cryst13030475.
[28] M. Yue, Y. Liu, G. He, L. Lian, Microstructure and mechanical performance of zirconium, manufactured by selective laser melting, Mater. Sci. Eng.: A 840 (2022) 1–8, https://doi.org/10.1016/j.msea.2022.142900.